CHEMISTRY OF MATERIALS

Article

pubs.acs.org/cm

Cathodoluminescence of Self-Organized Heterogeneous Phases in Multidimensional Perovskite Thin Films

Daniele Cortecchia,[†,‡] Kar Cheng Lew,[§,∥] Jin-Kyu So,[∥] Annalisa Bruno,[‡] and Cesare Soci*[,§,∥]

[†]Interdisciplinary Graduate School, Nanyang Technological University, Singapore 639798

[‡]Energy Research Institute @ NTU (ERI@N), Nanyang Technological University, 50 Nanyang Drive, Singapore 637553

[§]Division of Physics and Applied Physics, School of Physical and Mathematical Sciences, Nanyang Technological University, 21 Nanyang Link, Singapore 637371

[∥]Centre for Disruptive Photonic Technologies, TPI, Nanyang Technological University, Singapore 637371

Supporting Information

ABSTRACT: Multidimensional hybrid perovskites are becoming increasingly important for photovoltaic and light-emitting applications because of their improved moisture stability, unique luminescence, and transport properties. Little is known, however, about the phase distribution and self-organization properties of multidimensional perovskite thin films. In this work, we combine steady-state and time-resolved cathodoluminescence microscopy with photoluminescence techniques and reveal with unprecedented resolution the characteristic self-assembly of heterogeneous phases of perovskites with different dimensionality, driven by uneven redistribution of methylammonium cations during film formation. Our findings provide fundamental insights for the rational design of complex multidimensional perovskite systems with improved stability and emissive properties.

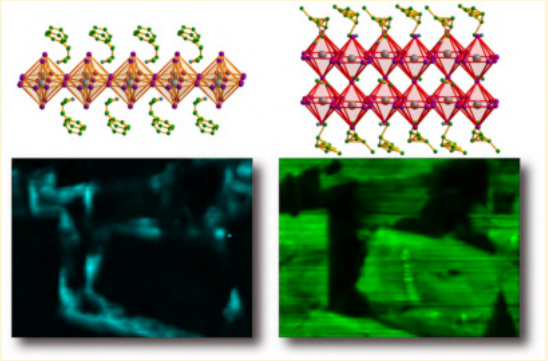

Three-dimensional (3D) hybrid perovskites have achieved breakthrough performances in both photovoltaic devices (with power conversion efficiencies now beyond 20%)[1] and light-emitting applications such as optically pumped lasers,[2,3] light-emitting diodes,[4,5] and field effect transistors.[6] Nevertheless, the fast degradation due to moisture uptake and temperature exposure is a serious issue that hinders the fabrication of devices with long-term stability.[7,8] Moreover, the small exciton binding energy characteristic of 3D hybrid perovskites makes trap-mediated, nonradiative recombination prevail under weak excitation densities and in the operational regime of standard electroluminescent devices. This leads to inefficient radiative recombination and a low photoluminescence quantum yield (PLQY), ultimately limiting the performance of light-emitting devices.[9,10]

In the last couple of years, hybrid perovskites of the Ruddlesden–Popper series have been successfully employed to overcome these issues and are currently emerging as the new frontier of functional materials.[11−13] With the general formula $(RNH_3)_2(A)_{n-1}[M_nX_{3n+1}]$ (where n is an integer), such hybrid perovskites combine a bulky aliphatic or aromatic ammonium cation (RNH_3) with a small cation A (e.g., methylammonium or formamidinium) and the metal halide network $[MX_6]^{4-}$, where M is a divalent metallic cation (e.g., Sn^{2+} or Pb^{2+}) and X is a halide (F^-, Cl^-, Br^-, or I^-). This combination typically results in a stack of alternating organic and inorganic layers, with the thickness of the inorganic sheets controlled by the reaction stoichiometry.[14] As a result, hybrid two-dimensional (2D)/3D systems are formed, which combine the high exciton binding energy of layered perovskites (~200−300 meV),[15] useful for reducing the level of thermal quenching and nonradiative recombination, with the unique high charge carrier mobility and long diffusion length of 3D systems. Moreover, the use of bulky and hydrophobic organic cations hampers water diffusion, enhancing the material's stability. Thus, this strategy is ideal for fabricating high-efficiency and stable devices based on both lead-based and lead-free multidimensional perovskites.[16−21] On the other hand, the combination of perovskites with increasing dimensionality in such hybrid 2D/3D systems results in electronic properties that cannot be achieved in single-phase 2D or 3D perovskites.[22] In particular, energy funneling from perovskite domains with a wider bandgap to those with a narrower bandgap can overcome the slow bimolecular recombination of 3D perovskites[9,23] and has allowed the fabrication of highly emissive LEDs with an external quantum efficiency between 8.8 and 11.7%.[24,25]

To date, a thorough understanding of the way in which these multidimensional perovskite systems self-organize into perovskite domains with heterogeneous phases is still lacking. Nonetheless, such knowledge is essential for synthetically engineering these multidimensional systems and further

Received: September 12, 2017
Revised: November 3, 2017
Published: November 3, 2017

DOI: 10.1021/acs.chemmater.7b03851
Chem. Mater. 2017, 29, 10088−10094

improving device performance. In this work, we studied the self-assembly and phase segregation of multidimensional perovskite systems via cathodoluminescence (CL) spectroscopy, exploiting its unrivaled spatial resolution. In CL spectroscopy, a focused electron beam creates localized optical excitations in materials down to the nanometer scale, which results in light emission over a broad electromagnetic spectrum.[26] CL spectroscopy has been widely used to study various forms of optical excitations in nanophotonic systems, such as plasmonic gratings,[27] nanoantennas,[28] photonic crystals,[29] metamaterials,[30] quantum emitters,[31,32] and nanoscale light sources.[33,34] Recently, the addition of time resolution capabilities to CL spectroscopy by adopting pulsed electron beams has also enabled the study of charge carrier dynamics at the nanoscale.[35] In perovskite systems, CL spectroscopy has revealed the local emission characteristics in 3D perovskites,[36,37] 2D perovskite crystals,[38] and the distribution of perovskites into hybrid matrices.[39]

As a representative multidimensional perovskite system, we have chosen the compounds of the series $(PEA)_2(MA)_{n-1}[Pb_nI_{3n+1}]$, grown in the form of single crystals and thin films, where PEA is phenethylammonium and MA is methylammonium. Perovskite single crystals were synthesized by adapting the procedure previously reported for the synthesis of *n*-butylammonium-based multidimensional perovskite. Phenethylamine, methylammonium chloride (MACl), and lead oxide (PbO) were mixed in hot concentrated hydroiodic acid (HI) water solutions at the desired stoichiometric ratio. Slow cooling of the mixture resulted in the crystallization of pure $(PEA)_2PbI_4$, $(PEA)_2(MA)[Pb_2I_7]$, and $MAPbI_3$ crystals, corresponding to the $n = 1$, $n = 2$, and $n = \infty$ compounds, respectively, of the series $(PEA)_2(MA)_{n-1}[Pb_nI_{3n+1}]$ (Figure 1a and Figure S1). $(PEA)_2PbI_4$ corresponds to the pure two-dimensional (2D) system in which single layers of PbI_6 octahedra alternate with double layers of phenethylammonium cations, while $MAPbI_3$ is the extreme case of the 3D perovskite made of the continuous network of corner-sharing PbI_6 octahedra.

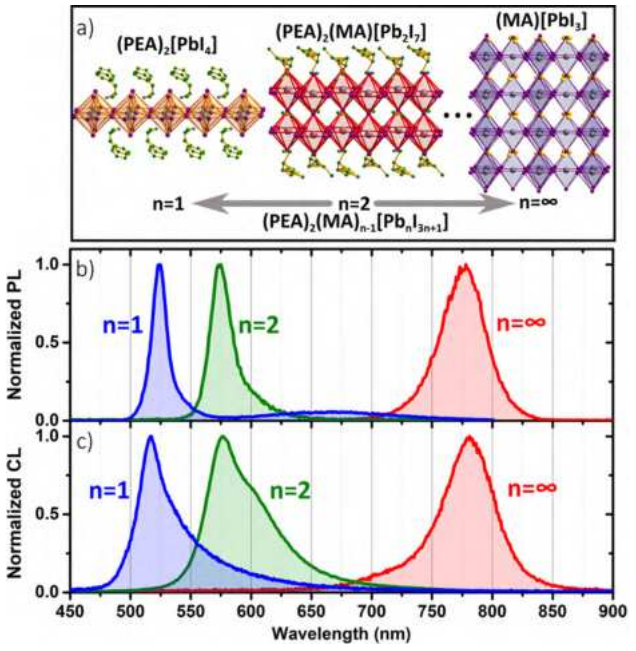

Figure 1. (a) Crystal structures of $(PEA)_2[PbI_4]$,[40] $(PEA)_2(MA)[Pb_2I_7]$,[40] and $MAPbI_3$[41] and corresponding normalized (b) photoluminescence and (c) cathodoluminescence spectra.

Photoluminescence (PL) measurements of the single crystals yielded peak emission wavelengths of 524, 574, and 778 nm for $n = 1$, $n = 2$, and $n = \infty$ compounds, respectively (Figure 1b). The red-shift of band-edge photoluminescence reflects bandgap narrowing in the $(PEA)_2(MA)_{n-1}[Pb_nI_{3n+1}]$ compounds with the increase in dimensionality.[12,25] The additional weak and broadband emission around 670 nm in the $n = 1$ compound might be attributed to the luminescence from self-trapped excitons or structure-induced emissive defects, as observed in other 2D perovskites.[15,42,43] The excitation of the single crystals by an electron beam (6 keV, 50 ms) produced cathodoluminescence at similar peak positions: 518, 576, and 780 nm (Figure 1c). The small shift between the PL and CL signal might be due to local inhomogeneity in different regions of the crystal.[44] In addition, the CL spectra are typically broader than the corresponding PL spectra, especially in the $n = 1$ and $n = 2$ perovskites, where a shoulder appears around 600 nm. CL band broadening is a consequence of the high-energy electron excitation leading to population of higher vibrational modes due to the thermal effect, as well as electron beam-induced defect formation in the perovskite.[45,46] Interestingly, the red-shifted photoluminescence band centered at 670 nm in the $n = 1$ perovskite (Figure 1b) is not visible in cathodoluminescence, indicating that excitation with an electron beam is followed by preferential radiative recombination through direct band-to-band transitions.

Single-phase perovskite films were fabricated by spin-coating, starting from solutions of the perovskite precursors in dimethyl sulfoxide (DMSO), which is a standard technique for the fabrication of highly efficient light-emitting devices based on multidimensional perovskites.[22,25] Single-phase films with $n = 1$ show the characteristic strong excitonic absorption typical of 2D perovskites peaked at 516 nm, and the corresponding excitonic luminescence at 524 nm (Figure 2a). Thin film X-ray diffraction confirmed the formation of single-phase $(PEA)_2PbI_4$ (monoclinic, space group $C2/m$), with a strong preferential orientation toward the ⟨200⟩ direction (Figure 2c). On the other hand, the addition of methylammonium to the spin-coated solution allows us to engineer the self-assembly of the multidimensional system. Films of multidimensional perovskites were obtained by mixing precursors (PEA)I, MAI, and PbI_2 in a 2:1:2 stoichiometric ratio; even though this ratio is the one required for the formation of the $n = 2$ phase $(PEA)_2(MA)[Pb_2I_7]$, a heterogeneous system is obtained. The formation of heterogeneous phases is facilitated by the presence of DMSO, a strong coordinating solvent that is known to slow crystallization by intercalating within the perovskite structure.[47]

The resulting film shows multiple excitonic peaks: two main bands at 516 and 568 nm related to the $n = 1$ and $n = 2$ phases, respectively, and two minor peaks at 607 and 644 nm related to the $n = 3$ and $n = 4$ compounds of the series, respectively. Accordingly, steady-state luminescence reveals the presence of two emission bands at 519 and 570 nm corresponding to the $n = 1$ and $n = 2$ band-edge emission, respectively, with the $(PEA)_2PbI_4$ luminescence being the dominating component. Perovskites with progressively higher dimensionality contribute to a minor extent to the emission beyond 600 nm, with an intensity that is ∼2 orders of magnitude weaker than that of the $n = 1$ emission (Figure 2b and Figure S2). The complex diffractogram was analyzed with a Pawley fit (Figure S3), which

DOI: 10.1021/acs.chemmater.7b03851
Chem. Mater. 2017, 29, 10088−10094

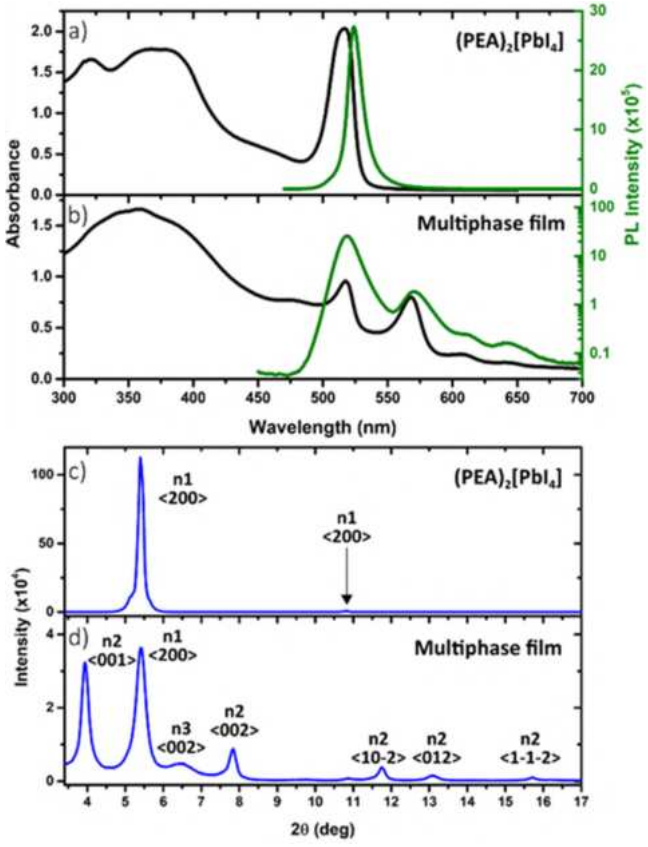

Figure 2. (a and b) Steady-state absorption (black) and photoluminescence (green) of $(PEA)_2PbI_4$ and multiphase thin films and (c and d) corresponding thin film X-ray diffraction patterns.

confirmed the presence of the two main, highly oriented $n = 1$ and $n = 2$ phases (triclinic, space group $P\bar{1}$), with the strongest diffraction peaks at 5.4° and 3.9°, respectively. Higher-order phases of the series (e.g., $n = 3$; triclinic, space group $P1$) could also be identified, with a much weaker diffraction peak at 6.5°.

To gain further insights into the compositional distribution of the multiphase films, we performed hyperspectral CL mapping by scanning the electron beam over a region of interest and synchronously recording the cathodoluminescence spectrum.[27] In the case of a polycrystalline film with a single $n = 1$ phase, the CL spectrum uniformly peaks around 520 nm, consistent with the emission of the corresponding single crystal, and is characterized by domains with brighter emission (Figure S4). On the other hand, multidimensional films show the formation of an ensemble of flat, platelike grains with an edge length of >10 μm (Figure 3a). These plates exhibit uniform morphology when imaged by atomic force microscopy (Figure S5). In the multicolor CL map (Figure 3b), the crystalline plates show emission that is stronger than that of intergrain regions, with blue-shifted luminescence compared to that from grain boundaries. This is more clearly seen in single-color CL maps for emission bands around 510, 580, and 720 nm (Figure 3c–e). For quantitative comparison, CL spectra from the representative locations indicated in Figure 3e are plotted in Figure 3f. The presence of the $n = 1$ phase in the intergrain regions near the plate edges (point A) is clearly identified by the emission around 510 nm. The characteristic emission of the $n = 2$ phase is observed from all over the plates (point B), with some local intensity variation (Figure 3d). In the intragrain regions (point C), a weak combined contribution of $n = 1$ and $n = 2$ phases is observed near the grain boundaries. The additional broadband emission in the range of 650–780 nm is attributed to the formation of $n \geq 3$ phases. In fewer different areas of the sample, the $n = 1$ phase does not form at the grain edges. Instead, the system is characterized by a more evident phase segregation in two different interconnected domains (Figure S6), consisting of perovskite clusters with lower and higher dimensionality, with CL peaked around 525 and 700

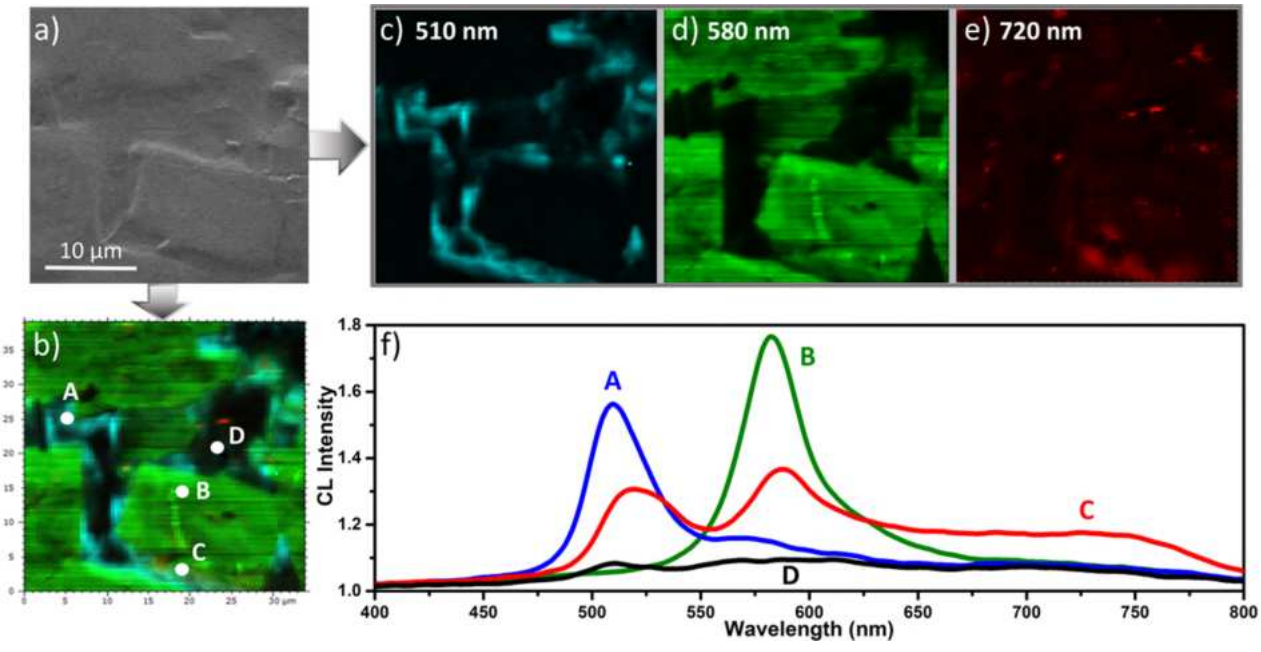

Figure 3. (a) Scanning electron microscope image of the multiphase $(PEA)_2(MA)_{n-1}[Pb_nI_{3n+1}]$ perovskite film and (b) corresponding cathodoluminescence (CL) map. (c–e) Single-color CL maps with components centered at 510, 580, and 720 nm, respectively. (f) Spatially resolved CL spectra at specific points of the CL map in panel b.

DOI: 10.1021/acs.chemmater.7b03851
Chem. Mater. 2017, 29, 10088–10094

nm, respectively. These observations imply the formation of MA^+ cation depletion regions near the grain edges during the crystallization of the $n = 2$ perovskite, leading to the preferential formation of the $n = 1$ phase at the grain edges. The remaining excess of MA^+ segregates at the intragrain regions, where it drives the formation of perovskites with higher dimensionality.

The recombination dynamics of multidimensional hybrid perovskite crystals and films were also studied by time-resolved photoluminescence and cathodoluminescence measurements (Figure 4). Time-resolved photoluminescence (TRPL) traces

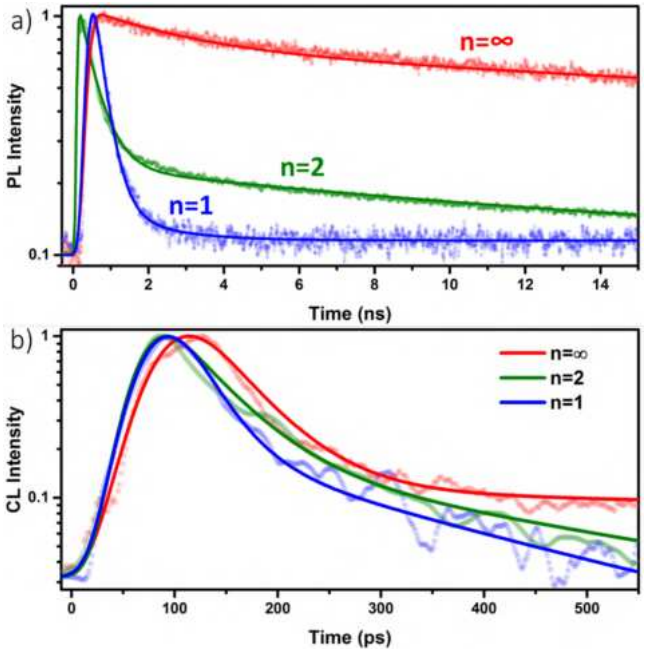

Figure 4. Time-resolved measurement of perovskite single crystals. (a) TRPL traces of emission bands centered at 525, 575, and 780 nm for $n = 1$, $n = 2$, and $n = \infty$, respectively (λ_{exc} = 400 nm). (b) TRCL traces of emission bands at 525, 575, and 780 nm for $n = 1$, $n = 2$, and $n = \infty$, respectively.

of $n = 1$, $n = 2$, and $n = \infty$ single crystals show a double-exponential decay with a fast and a slow decay component, whose overall lifetime increases with perovskite dimensionality (Table 1). The fast decay component (τ_1) increases from 298 ps for $n = 1$ to 2660 ps for $n = \infty$, while its amplitude decreases significantly with dimensionality. The slow decay component becomes dominant at a higher dimensionality, exceeding 40 ns

Table 1. Time-Resolved Photoluminescence (TRPL) and Cathodoluminescence (TRCL) Fitting Parameters for Perovskite Single Crystals[a]

crystal	λ (nm)	A_1	τ_1 (ps)	A_2	τ_2 (ps)
		Time-Resolved PL			
$n = \infty$	780	0.36	2657	0.64	44298
$n = 2$	575	0.83	450	0.17	14184
$n = 1$	525	0.97	298	0.03	1417
		Time-Resolved CL			
$n = \infty$	780	0.96	50	0.04	2059
$n = 2$	575	0.89	49	0.11	380
$n = 1$	525	0.92	34	0.08	319

[a]TRPL decays are collected with a 400 nm excitation wavelength. τ is the characteristic lifetime, and A is the amplitude.

for the $n = \infty$ phase (see Table 1). In the time-resolved mode, transient CL was produced by a pulsed electron beam (~10 ps, 80 MHz) and a streak camera was used for the time-domain analysis of the collected CL. During the measurement, the electron beam was raster scanned continuously over a 30 μm × 30 μm area. In comparison with TRPL, time-resolved cathodoluminescence (TRCL) could reveal a much faster decay component (τ_1), which is 34 ps for $n = 1$ and ~50 ps for $n = 2$ and $n = \infty$ (Table 1). This could not be resolved in TRPL measurements because of the time-resolution limitation of our setup. We attribute the ultrafast decay to hot exciton thermalization and Auger recombination.[48,49] The slow components extracted from TRCL traces (τ_2) match well the fast components (τ_1) of TRPL traces, suggesting that they originate from the same process. Because of the limitation in the streaking unit, decays beyond 2 ns could not be probed in TRCL measurements.

The luminescence dynamics of multiphase films could be clearly visualized in the TRCL streak maps (Figure 5).

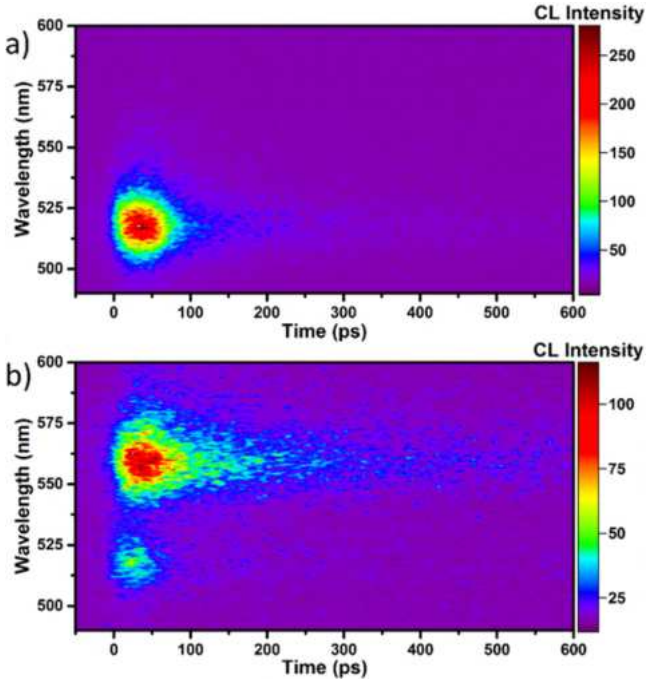

Figure 5. TRCL maps of perovskite films: (a) $(PEA)_2PbI_4$ and (b) $(PEA)_2(MA)_{n-1}[Pb_nI_{3n+1}]$ multiphase thin film.

Consistent with steady-state CL results, the single-phase film ($n = 1$) shows a single CL peak at 520 nm (Figure 5a), while the multiphase film (described in Figure 3) shows two pronounced CL peaks around 520 nm (short-lived) and 565 nm (long-lived), corresponding to the $n = 1$ and $n = 2$ phases, respectively (Figure 5b). In the multiphase film, the CL from higher-order phases was not intense enough to be detected in TRCL mode. For quantitative analysis, TRCL decay traces were produced by integrating the streak map in Figure 5 around the maximum of the relevant emission bands (Figure S7) and fitted to double-exponential curves. The obtained fitting parameters are summarized in Table 2. The emission from the $n = 1$ phase in the multiphase film (520 nm) decays faster than that in the single crystal or single-phase film by ~40% (see Tables 1 and 2). This partial quenching of the $n = 1$ luminescence can be attributed to the transfer of energy from

DOI: 10.1021/acs.chemmater.7b03851
Chem. Mater. 2017, 29, 10088−10094

Table 2. Time-Resolved Cathodoluminescence (TRCL) Fitting Parameters for Perovskite Films of $(PEA)_2PbI_4$ (n = 1; λ_{probe} = 520 nm) and Multiphase $(PEA)_2(MA)_{n-1}[Pb_nI_{3n+1}]$ Films (λ_{probe} = 520 and 565 nm)[a]

Thin Film	λ_{probe} (nm)	A_1	τ_1 (ps)	A_2	τ_2 (ps)
n = 1	*520*	*0.96*	*31*	*0.04*	*308*
multiphase	520	0.92	18	0.08	135
	565	0.91	48	0.09	486

[a] τ is the characteristic lifetime, and A is the amplitude.

the n = 1 phase to higher-order phases with narrower bandgaps,[9,25] where the transfer of energy to the n = 2 phase is expected to dominate because of its proximity to the n = 1 phase (see Figure 3).

In conclusion, we have shown that multidimensional perovskites of the Ruddlesden–Popper series can form a highly complex system upon deposition of thin films. Unlike the synthesis of single crystals, the composition of thin films is not solely dictated by the reaction stoichiometry; it is rather the result of self-organization of heterogeneous phases with well-defined patterns. The unrivaled spatial resolution of CL spectroscopy revealed that the n = 1 perovskite self-assembles preferentially near the edges of crystalline grains of the n = 2 phase, while promoting the formation of perovskites with higher dimensionality in the intergrain regions. The self-assembled heterogeneous structures in such films strongly affect light-emitting properties and recombination dynamics, leading to partial quenching of the n = 1 perovskite luminescence. This is likely due to the transfer of energy to perovskite domains with higher dimensionality, predominantly the n = 2 phase that is in direct contact with the n = 1 phase. Understanding the self-organization properties of multidimensional perovskites will be of primary importance for fostering the design of materials with improved moisture stability as well as luminescence efficiency.[22,25] For example, thin 2D perovskite layers enclosing perovskite grains with higher dimensionality could be designed to act as a barrier to moisture diffusion, with minimal effect on the material's transport properties. Similarly, the domain size, type, and connectivity of the heterogeneous phase could be adjusted by controlling the reaction's parameters and processing conditions to optimize the energy transfer process toward specific perovskite domains.

■ ASSOCIATED CONTENT

Supporting Information

The Supporting Information is available free of charge on the ACS Publications website at DOI: 10.1021/acs.chemmater.7b03851.

Experimental methods and Figures S1–S7 (PDF)

■ AUTHOR INFORMATION

Corresponding Author

*E-mail: csoci@ntu.edu.sg.

ORCID

Cesare Soci: 0000-0002-0149-9128

Author Contributions

D.C. and K.C.L. contributed equally to this work. D.C. fabricated and characterized the samples and drafted the manuscript. K.C.L. and J.-K.S. performed CL measurements. A.B. performed PL measurements. C.S. supervised the work and provided guidance. All authors discussed the results and contributed to the preparation of the manuscript.

Notes

The authors declare no competing financial interest.

■ ACKNOWLEDGMENTS

This work was supported by the Ministry of Education (MOE2016-T1-1-164 and MOE2011-T3-1-005) and the National Research Foundation (NRF-CRP14-2014-03) of Singapore. The authors also acknowledge support from the Nanyang Technological University Strategic Research Facilities Initiative.

■ ABBREVIATIONS

PEA, phenethylammonium; MA, methylammonium; PL, photoluminescence; DMSO, dimethyl sulfoxide; CL, cathodoluminescence; TR, time-resolved.

■ REFERENCES

(1) Li, X.; Bi, D.; Yi, C.; Décoppet, J.-D.; Luo, J.; Zakeeruddin, S. M.; Hagfeldt, A.; Grätzel, M. A vacuum flash–assisted solution process for high-efficiency large-area perovskite solar cells. *Science* **2016**, *353*, 58–62.

(2) Xing, G.; Mathews, N.; Lim, S. S.; Yantara, N.; Liu, X.; Sabba, D.; Grätzel, M.; Mhaisalkar, S.; Sum, T. C. Low-temperature solution-processed wavelength-tunable perovskites for lasing. *Nat. Mater.* **2014**, *13*, 476–480.

(3) Deschler, F.; Price, M.; Pathak, S.; Klintberg, L. E.; Jarausch, D.-D.; Higler, R.; Hüttner, S.; Leijtens, T.; Stranks, S. D.; Snaith, H. J.; Atatüre, M.; Phillips, R. T.; Friend, R. H. High Photoluminescence Efficiency and Optically Pumped Lasing in Solution-Processed Mixed Halide Perovskite Semiconductors. *J. Phys. Chem. Lett.* **2014**, *5*, 1421–1426.

(4) Cho, H.; Jeong, S.-H.; Park, M.-H.; Kim, Y.-H.; Wolf, C.; Lee, C.-L.; Heo, J. H.; Sadhanala, A.; Myoung, N.; Yoo, S.; Im, S. H.; Friend, R. H.; Lee, T.-W. Overcoming the electroluminescence efficiency limitations of perovskite light-emitting diodes. *Science* **2015**, *350*, 1222–1225.

(5) Adjokatse, S.; Fang, H.-H.; Loi, M. A. Broadly tunable metal halide perovskites for solid-state light-emission applications. *Mater. Today* **2017**, *20*, 413.

(6) Chin, X. Y.; Cortecchia, D.; Yin, J.; Bruno, A.; Soci, C. Lead iodide perovskite light-emitting field-effect transistor. *Nat. Commun.* **2015**, *6*, 7383.

(7) Berhe, T. A.; Su, W.-N.; Chen, C.-H.; Pan, C.-J.; Cheng, J.-H.; Chen, H.-M.; Tsai, M.-C.; Chen, L.-Y.; Dubale, A. A.; Hwang, B.-J. Organometal halide perovskite solar cells: degradation and stability. *Energy Environ. Sci.* **2016**, *9*, 323–356.

(8) Bruno, A.; Cortecchia, D.; Chin, X. Y.; Fu, K.; Boix, P. P.; Mhaisalkar, S.; Soci, C. Temperature and Electrical Poling Effects on Ionic Motion in $MAPbI_3$ Photovoltaic Cells. *Adv. Energy Mater.* **2017**, *7*, 1700265.

(9) Xing, G.; Wu, B.; Wu, X.; Li, M.; Du, B.; Wei, Q.; Guo, J.; Yeow, E. K. L.; Sum, T. C.; Huang, W. Transcending the slow bimolecular recombination in lead-halide perovskites for electroluminescence. *Nat. Commun.* **2017**, *8*, 14558.

(10) Sutherland, B. R.; Sargent, E. H. Perovskite photonic sources. *Nat. Photonics* **2016**, *10*, 295–302.

(11) Saidaminov, M. I.; Mohammed, O. F.; Bakr, O. M. Low-Dimensional-Networked Metal Halide Perovskites: The Next Big Thing. *ACS Energy Lett.* **2017**, *2*, 889–896.

(12) Stoumpos, C. C.; Cao, D. H.; Clark, D. J.; Young, J.; Rondinelli, J. M.; Jang, J. I.; Hupp, J. T.; Kanatzidis, M. G. Ruddlesden–Popper Hybrid Lead Iodide Perovskite 2D Homologous Semiconductors. *Chem. Mater.* **2016**, *28*, 2852–2867.

(13) Blancon, J.-C.; Tsai, H.; Nie, W.; Stoumpos, C. C.; Pedesseau, L.; Katan, C.; Kepenekian, M.; Soe, C. M. M.; Appavoo, K.; Sfeir, M. Y.; Tretiak, S.; Ajayan, P. M.; Kanatzidis, M. G.; Even, J.; Crochet, J. J.;

DOI: 10.1021/acs.chemmater.7b03851
Chem. Mater. 2017, 29, 10088–10094

Mohite, A. D. Extremely efficient internal exciton dissociation through edge states in layered 2D perovskites. *Science* **2017**, *355*, 1288.
(14) Saparov, B.; Mitzi, D. B. Organic−Inorganic Perovskites: Structural Versatility for Functional Materials Design. *Chem. Rev.* **2016**, *116*, 4558−4596.
(15) Cortecchia, D.; Neutzner, S.; Srimath Kandada, A. R.; Mosconi, E.; Meggiolaro, D.; De Angelis, F.; Soci, C.; Petrozza, A. Broadband Emission in Two-Dimensional Hybrid Perovskites: The Role of Structural Deformation. *J. Am. Chem. Soc.* **2017**, *139*, 39−42.
(16) Quan, L. N.; Yuan, M.; Comin, R.; Voznyy, O.; Beauregard, E. M.; Hoogland, S.; Buin, A.; Kirmani, A. R.; Zhao, K.; Amassian, A.; Kim, D. H.; Sargent, E. H. Ligand-Stabilized Reduced-Dimensionality Perovskites. *J. Am. Chem. Soc.* **2016**, *138*, 2649−2655.
(17) Cao, D. H.; Stoumpos, C. C.; Yokoyama, T.; Logsdon, J. L.; Song, T.-B.; Farha, O. K.; Wasielewski, M. R.; Hupp, J. T.; Kanatzidis, M. G. Thin Films and Solar Cells Based on Semiconducting Two-Dimensional Ruddlesden−Popper $(CH_3(CH_2)_3NH_3)_2(CH_3NH_3)_{n-1}Sn_nI_{3n+1}$ Perovskites. *ACS Energy Lett.* **2017**, *2*, 982−990.
(18) Grancini, G.; Roldán-Carmona, C.; Zimmermann, I.; Mosconi, E.; Lee, X.; Martineau, D.; Narbey, S.; Oswald, F.; De Angelis, F.; Graetzel, M.; Nazeeruddin, M. K. One-Year stable perovskite solar cells by 2D/3D interface engineering. *Nat. Commun.* **2017**, *8*, 15684.
(19) Tsai, H.; Nie, W.; Blancon, J.-C.; Stoumpos, C. C.; Asadpour, R.; Harutyunyan, B.; Neukirch, A. J.; Verduzco, R.; Crochet, J. J.; Tretiak, S.; Pedesseau, L.; Even, J.; Alam, M. A.; Gupta, G.; Lou, J.; Ajayan, P. M.; Bedzyk, M. J.; Kanatzidis, M. G.; Mohite, A. D. High-efficiency two-dimensional Ruddlesden−Popper perovskite solar cells. *Nature* **2016**, *536*, 312−316.
(20) Smith, I. C.; Hoke, E. T.; Solis-Ibarra, D.; McGehee, M. D.; Karunadasa, H. I. A Layered Hybrid Perovskite Solar-Cell Absorber with Enhanced Moisture Stability. *Angew. Chem.* **2014**, *126*, 11414−11417.
(21) Shao, S.; Liu, J.; Portale, G.; Fang, H.-H.; Blake, G. R.; ten Brink, G. H.; Koster, L. J. A.; Loi, M. A. Highly Reproducible Sn-Based Hybrid Perovskite Solar Cells with 9% Efficiency. *Adv. Energy Mater.* **2017**, 1702019.
(22) Quan, L. N.; Zhao, Y.; García de Arquer, F. P.; Sabatini, R.; Walters, G.; Voznyy, O.; Comin, R.; Li, Y.; Fan, J. Z.; Tan, H.; Pan, J.; Yuan, M.; Bakr, O. M.; Lu, Z.; Kim, D. H.; Sargent, E. H. Tailoring the Energy Landscape in Quasi-2D Halide Perovskites Enables Efficient Green-Light Emission. *Nano Lett.* **2017**, *17*, 3701−3709.
(23) Neutzner, S.; Srimath Kandada, A. R.; Lanzani, G.; Petrozza, A. A dual-phase architecture for efficient amplified spontaneous emission in lead iodide perovskites. *J. Mater. Chem. C* **2016**, *4*, 4630−4633.
(24) Wang, N.; Cheng, L.; Ge, R.; Zhang, S.; Miao, Y.; Zou, W.; Yi, C.; Sun, Y.; Cao, Y.; Yang, R.; Wei, Y.; Guo, Q.; Ke, Y.; Yu, M.; Jin, Y.; Liu, Y.; Ding, Q.; Di, D.; Yang, L.; Xing, G.; Tian, H.; Jin, C.; Gao, F.; Friend, R. H.; Wang, J.; Huang, W. Perovskite light-emitting diodes based on solution-processed self-organized multiple quantum wells. *Nat. Photonics* **2016**, *10*, 699−704.
(25) Yuan, M.; Quan, L. N.; Comin, R.; Walters, G.; Sabatini, R.; Voznyy, O.; Hoogland, S.; Zhao, Y.; Beauregard, E. M.; Kanjanaboos, P.; Lu, Z.; Kim, D. H.; Sargent, E. H. Perovskite energy funnels for efficient light-emitting diodes. *Nat. Nanotechnol.* **2016**, *11*, 872−877.
(26) García de Abajo, F. J. Optical excitations in electron microscopy. *Rev. Mod. Phys.* **2010**, *82*, 209−275.
(27) Bashevoy, M.; Jonsson, F.; MacDonald, K.; Chen, Y.; Zheludev, N. Hyperspectral imaging of plasmonic nanostructures with nanoscale resolution. *Opt. Express* **2007**, *15*, 11313−11320.
(28) Denisyuk, A.; Adamo, G.; MacDonald, K.; Edgar, J.; Arnold, M.; Myroshnychenko, V.; Ford, M.; García de Abajo, F. J.; Zheludev, N. Transmitting Hertzian optical nanoantenna with free-electron feed. *Nano Lett.* **2010**, *10*, 3250−3252.
(29) Sapienza, R.; Coenen, T.; Renger, J.; Kuttge, M.; van Hulst, N.; Polman, A. Deep-subwavelength imaging of the modal dispersion of light. *Nat. Mater.* **2012**, *11*, 781−787.
(30) Adamo, G.; Ou, J. Y.; So, J. K.; Jenkins, S. D.; De Angelis, F.; MacDonald, K. F.; Di Fabrizio, E.; Ruostekoski, J.; Zheludev, N. I. Electron-Beam-Driven Collective-Mode Metamaterial Light Source. *Phys. Rev. Lett.* **2012**, *109*, 217401.
(31) Tikhomirov, V.; Adamo, G.; Nikolaenko, A.; Rodriguez, V.; Gredin, P.; Mortier, M.; Zheludev, N.; Moshchalkov, V. Cathodo-and photoluminescence in Yb^{3+}-Er^{3+} co-doped PbF_2 nanoparticles. *Opt. Express* **2010**, *18*, 8836−8846.
(32) Merano, M.; Sonderegger, S.; Crottini, A.; Collin, S.; Renucci, P.; Pelucchi, E.; Malko, A.; Baier, M.; Kapon, E.; Deveaud, B.; Ganière, J.-D. Probing carrier dynamics in nanostructures by picosecond cathodoluminescence. *Nature* **2005**, *438*, 479−482.
(33) Adamo, G.; MacDonald, K. F.; Fu, Y.; Wang, C.; Tsai, D.; García de Abajo, F. J.; Zheludev, N. Light well: a tunable free-electron light source on a chip. *Phys. Rev. Lett.* **2009**, *103*, 113901.
(34) Li, G.; Clarke, B. P.; So, J. K.; MacDonald, K. F.; Zheludev, N. I. Holographic free-electron light source. *Nat. Commun.* **2016**, *7*, 13705.
(35) Merano, M.; Sonderegger, S.; Crottini, A.; Collin, S.; Renucci, P.; Pelucchi, E.; Malko, A.; Baier, M. H.; Kapon, E.; Deveaud, B.; Ganiere, J. D. Probing carrier dynamics in nanostructures by picosecond cathodoluminescence. *Nature* **2005**, *438*, 479−482.
(36) Dar, M. I.; Jacopin, G.; Hezam, M.; Arora, N.; Zakeeruddin, S. M.; Deveaud, B.; Nazeeruddin, M. K.; Grätzel, M. Asymmetric Cathodoluminescence Emission in $CH_3NH_3PbI_{3-x}Br_x$ Perovskite Single Crystals. *ACS Photonics* **2016**, *3*, 947−952.
(37) Hentz, O.; Zhao, Z.; Gradečak, S. Direct correlation between local stoichiometry and optoelectronic properties in $CH_3NH_3PbI_3$ films. *2016 IEEE 43rd Photovoltaic Specialists Conference (PVSC)*, June 5−10, 2016; IEEE: New York, 2016, pp 3661−3663.
(38) Dou, L.; Wong, A. B.; Yu, Y.; Lai, M.; Kornienko, N.; Eaton, S. W.; Fu, A.; Bischak, C. G.; Ma, J.; Ding, T.; Ginsberg, N. S.; Wang, L.-W.; Alivisatos, A. P.; Yang, P. Atomically thin two-dimensional organic-inorganic hybrid perovskites. *Science* **2015**, *349*, 1518−1521.
(39) Vassilakopoulou, A.; Papadatos, D.; Koutselas, I. Flexible, cathodoluminescent and free standing mesoporous silica films with entrapped quasi-2D perovskites. *Appl. Surf. Sci.* **2017**, *400*, 434−439.
(40) Calabrese, J.; Jones, N. L.; Harlow, R. L.; Herron, N.; Thorn, D. L.; Wang, Y. Preparation and characterization of layered lead halide compounds. *J. Am. Chem. Soc.* **1991**, *113*, 2328−2330.
(41) Stoumpos, C. C.; Malliakas, C. D.; Kanatzidis, M. G. Semiconducting Tin and Lead Iodide Perovskites with Organic Cations: Phase Transitions, High Mobilities, and Near-Infrared Photoluminescent Properties. *Inorg. Chem.* **2013**, *52*, 9019−9038.
(42) Cortecchia, D.; Yin, J.; Bruno, A.; Lo, S.-Z. A.; Gurzadyan, G. G.; Mhaisalkar, S.; Bredas, J.-L.; Soci, C. Polaron self-localization in white-light emitting hybrid perovskites. *J. Mater. Chem. C* **2017**, *5*, 2771−2780.
(43) Neogi, I.; Bruno, A.; Bahulayan, D.; Goh, T. W.; Ghosh, B.; Ganguly, R.; Cortecchia, D.; Sum, T. C.; Soci, C.; Mathews, N.; Mhaisalkar, S. G. Broadband-emitting 2D hybrid organic−inorganic perovskite based on cyclohexane-bis(methylamonium) cation. *ChemSusChem* **2017**, *10*, 3765−3772.
(44) El-Hajje, G.; Momblona, C.; Gil-Escrig, L.; Avila, J.; Guillemot, T.; Guillemoles, J.-F.; Sessolo, M.; Bolink, H. J.; Lombez, L. Quantification of spatial inhomogeneity in perovskite solar cells by hyperspectral luminescence imaging. *Energy Environ. Sci.* **2016**, *9*, 2286−2294.
(45) Klein-Kedem, N.; Cahen, D.; Hodes, G. Effects of Light and Electron Beam Irradiation on Halide Perovskites and Their Solar Cells. *Acc. Chem. Res.* **2016**, *49*, 347−354.
(46) Xiao, C.; Li, Z.; Guthrey, H.; Moseley, J.; Yang, Y.; Wozny, S.; Moutinho, H.; To, B.; Berry, J. J.; Gorman, B.; Yan, Y.; Zhu, K.; Al-Jassim, M. Mechanisms of Electron-Beam-Induced Damage in Perovskite Thin Films Revealed by Cathodoluminescence Spectroscopy. *J. Phys. Chem. C* **2015**, *119*, 26904−26911.
(47) Jeon, N. J.; Noh, J. H.; Kim, Y. C.; Yang, W. S.; Ryu, S.; Seok, S. I. Solvent engineering for high-performance inorganic−organic hybrid perovskite solar cells. *Nat. Mater.* **2014**, *13*, 897−903.
(48) Herz, L. M. Charge-Carrier Dynamics in Organic-Inorganic Metal Halide Perovskites. *Annu. Rev. Phys. Chem.* **2016**, *67*, 65−89.

DOI: 10.1021/acs.chemmater.7b03851
Chem. Mater. 2017, 29, 10088−10094

(49) Yacobi, B. G.; Holt, D. B. *Cathodoluminescence Microscopy of Inorganic Solids*; Springer: New York, 2013.

DOI: 10.1021/acs.chemmater.7b03851
Chem. Mater. 2017, 29, 10088−10094